End-ring wear in deep well submersible motor pumps

Jorge Bonet-Jara, Daniel Morinigo-Sotelo, *Member, IEEE*, Oscar Duque-Perez, Luis Serrano-Iribarnegaray and Joan Pons-Llinares, *Member, IEEE*

***Abstract*—Wear of end-ring is to date an unreported and uninvestigated failure that very frequently takes place in deep well submersible motor pumps. The present paper first analyses the particularities of these induction motors, especially their unusual rotor manufacturing process. Failure mechanism related to the end-ring wear is described, showing several examples of damaged rotors in a motor repair shop. Then, the difficulties of its diagnosis through conventional rotor asymmetry indicators are described, caused by the subtlety of this fault and the very easy appearance of false negatives. The end-ring wear detection through a multicomponent approach is researched through simulation, laboratory results and the diagnosis of two field motors showing that new fault alarm levels need to be defined. To perform this last step and for the first time in the technical literature, two induction motors working in a deep borehole have been continuously monitored (one measure every six operating hours) for almost one year.**

***Index Terms*—Diagnosis, induction motor, pump, false negative, end-ring**

I. Introduction

The type of rotor faults in induction motors highly depends on the rotor manufacturing process [1]. In the case of copper or aluminium fabricated rotors, the failure mainly consists in the breakage of the bar (typically at the joint with the end-ring), and its detachment from it [2]. Once the rotor core is assembled in these motors, putting together a set of thin ferromagnetic laminations, previously copper or aluminium fabricated bars are inserted in the lamination holes and swaged. The bars slightly exceed the rotor core and are shortcircuited by brazing or welding them to an end-ring (a previously fabricated solid circumferential piece of copper or aluminium). A certain space is left between the end-ring and the rotor core, where the bars can be clearly seen. In that space is where the bar breaks and detaches from the end-ring [3]. In the case of die-cast aluminium, bars and end-ring are moulded altogether with the rotor core, being its main failure porosity or melting [4], since when end-rings and bars form a unique piece, crack and detachment problems disappear.

J. Bonet-Jara and J. Pons-Llinares are with the Instituto Tecnológico de la Energía, Universitat Politècnica de València, C/Camino de Vera s/n, 46022, València, Spain (e-mail: jorboja@die.upv.es; jpons@die.upv.es).

L. Serrano-Iribarnegaray is with the Departamento de Ingeniería Eléctrica, Universitat Politècnica de València, C/Camino de Vera s/n, 46022, València, Spain (e-mail: lserrano@die.upv.es).

D. Morinigo-Sotelo and O. Duque-Perez are with Research Group Adire, Instituto de Tecnologías Aplicadas a la Produccción (ITAP), Universidad de Valladolid, 47009, Valladolid, Spain (e-mail: daniel.morinigo@eii.uva.es; oscar.duque@eii.uva.es)

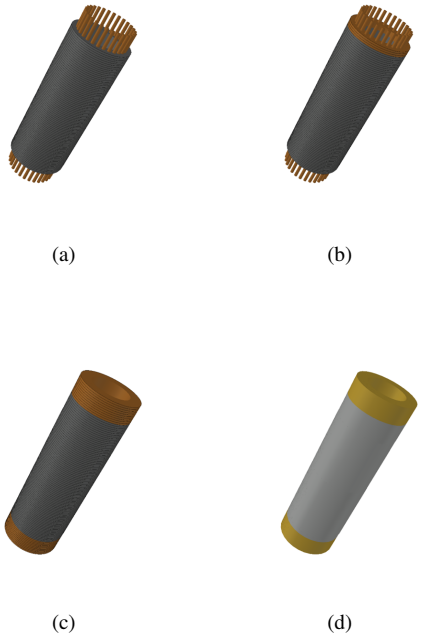

Fig. 1. Rotor assembly of a deep well submersible motor: copper bars with ferromagnetic laminations (a); some (b) and all (c) of the copper sheets of the end-ring and its final copper liquid soldering plus the paint coating (d).

Rotor cage failure accounts for 5-15 % of induction motor failures [5]. Nevertheless, none or very few are related to the breakage of the end-ring itself. As analysed in the present paper, the type of failure in deep well submersible motor pumps is very different. These motors use previously fabricated copper bars, but instead of being a solid piece, the end-ring is made of several copper sheets with the same shape as the ferromagnetic laminations. These sheets are stacked until they cover the bar endings that remain out of the rotor core. Then, the gaps between the end-ring sheets and the bars are filled with liquid copper soldering, and a coat of paint is applied to the rotor. This assembly process is shown in Fig. 1.

As will be demonstrated with several real field cases throughout the article, the end ring wears very often due to internal cooling water and high-speed rotation. The liquid copper solder, which unites the bars and end-ring sheets, gradually losses material until the copper sheets appear. Then, pieces of the copper sheets themselves might detach, expos-

ing the bars which are initially covered. At the beginning of the failure mechanism, wear appears on some end-ring segments, being too subtle to be detected. Then, the unequal wear uniformly extends to the whole end-ring, cancelling the initial asymmetry, which might cause the appearance of a false negative. Concluding, the detection of this type of failure is a challenging problem.

No papers have investigated end-ring wear and very few address end-ring breakage. It has been stated that broken end-ring segments cause a periodic fluctuation in the line current and rotor speed [6] (basis of rotor asymmetries detection via current spectrum). More precisely, end-ring faults produce the same harmonic components in the stator line current as rotor bar faults [7]. This has been confirmed by simulation using models of induction motors based on inductances calculation [8] and Finite Element Methods [9]; it has also been proven through simulation the appearance of harmonics in torque and speed [10].

Since in conventional motors, end-ring breakage is much less frequent than bar breakage, most studies focus on the latter failure. On the other hand, as stated through the paper, end-ring wear (typical of deep well motors) always causes false negatives. Therefore, to find similarities, it is important to survey the false negative caused by non-adjacent broken bars (which might also cancel rotor asymmetry) when only the Lower Sideband Harmonic (LSH) is monitored [11]–[13]. To solve the problem of false negatives, some authors propose to monitor fault harmonics different than LSH [14], [15]. Instead of using a single current, other authors have proposed to obtain the phase currents to calculate the zero-sequence current [16] and Park's vector [17], or analyse the spectrum of other magnitudes as the flux [18]–[21]. Nevertheless, phase currents are not always available for motors submerged at least 50 m, while it is impossible to measure the flux. Finally, only one paper shows the possible appearance of false negatives under several broken end-rings [22].

This paper, which is an extended version of the contribution presented at the IEEE 13th international SDEMPED conference [23], is the first in which end-ring wear in deep well submersible pump motors is investigated, which is a challenging problem due to the subtle appearance of the failure at its beginning, and the possible occurrence of false negatives when severity increases. Its detection is crucial in deep well motors predictive maintenance since end-ring wear highly contaminates the water that internally cools the motor, increasing the chances to cause secondary damage in bearings and stator insulation.

II. Deep well submersible motor pumps: special features and failure mechanism.

The rotor manufacturing process for this type of motor, and particularly its end-ring, has been explained in the introduction. The widespread end-ring wear problem has also been presented. In this section, the end-ring wear failure mechanism is described using real field cases of damaged rotors (pictures from the motor repair shop are presented).

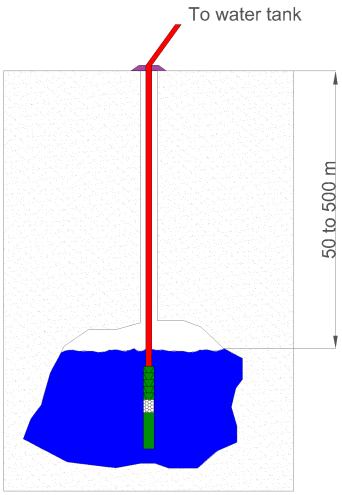

Fig. 2. Motor-pump set submerged in an aquifer with a 50 to 500 m piping elevating the water to a tank.

Previously, the unique features of this type of motor are synthesised:

A. Special features of induction motors in deep well submersible pumps.

Submersible pumps are mainly used for water supply extracted from aquifers at depths from 50 to 500 m (Fig. 2) where the motor-pump set elevates the water to a tank through a pipeline. The motor-pump set works submerged in the aquifer, with the motor-pump shafts directly coupled and in vertical position (the motor underneath the pump and the water inlet between them). Sometimes, to externally cool the motor, a metal cover is placed embracing the motor to force water to flow between the cover and the motor surface before entering the inlet (Fig. 3). The motor frame, which is smooth and without heat sinks, is internally cooled by pre-filling with a mixture of water and glycol. Carbon or stainless steel thrust bearings are used to support the weight of the entire assembly.

The borehole drilled to reach the aquifer has a small diameter to reduce excavation costs. This determines the motor design with a small diameter, together with the insulation needed for underwater operation. Rotor cage with skewed bars induction motors are used, with a length proportionally high compared with its small diameter. One-pole pairs design is used to achieve high power with a reduced motor size, as its high rotating speed increases output hydraulic power, but also components wear. Motors are fed at least with a soft-starter to prevent startup peak currents and preferably with a frequency converter, which also permits to adjust the pump speed. Nowadays, all new motors are converter-fed. Motors are operated at a fixed speed, without significant load or grid oscillations; therefore, FFT signal analysis can be applied for monitoring purposes.

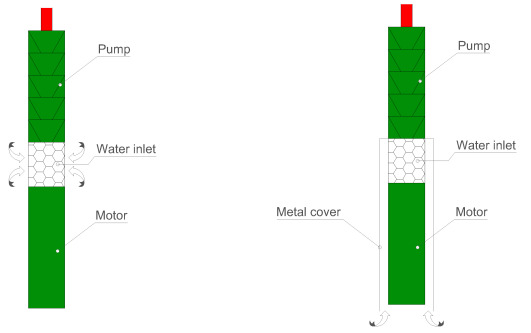

(a) (b)

Fig. 3. Motor-pump set without (a) and with (b) metal cover to force water flowing through the motor surface before entering the water inlet.

B. Failure mechanism of deep well submersible motor rotor.

As stated in the introduction, once manufactured, the copper rotor structure is very similar to an Al die cast rotor (without porosity problems). Therefore, rotor bars cannot break as they do in standard copper rotors. The only rotor asymmetry that might take place is caused by the degradation of the end-ring liquid soldering, which glues the copper laminations and the bars together, constituting the end-ring. The internally cooling water flows in contact with the rotor and stator windings. The copper liquid soldering is especially delicate and very often starts to lose material. Water is propelled by the rotor, which rotates at a high-speed (due to the use of one-pole pairs), boosting the liquid soldering erosion: its degradation causes wear in the end-ring segments between the bars, together with loss of contact between the bars inserted in the lamination end-rings. Fig. 4 shows photos of several rotor end-rings in a motor repair shop: new (a) and with different degrees of wear in (b), (c) and (d). Water suspended particles, detached from the rotor, are shoot to the inner part of the stator by the centrifuge force. Some of these particles might impact the winding, breaking the insulation, which is what usually happens when parts of a rotor bar are detached in standard copper rotor induction motors.

End-ring wear is not easy to be detected. Even if wear starts on some point of the end-ring (for instance, in a segment between two bars), it will spread over the whole end-ring; then, the process starts again, increasing the wear in another segment gradually spreading to the rest of the end-ring. Initially, the wear may be too subtle to cause fault harmonics to appear in the line current, making detection impossible. Once the failure has expanded to other segments, the effects may be cancelled out, leading to the appearance of false negatives.

Concluding, end-ring wear is a widespread failure in induction motors of submersible pumps (unlike end-ring breakage in standard induction motors), which might cause severe secondary damage in other components. It is difficult to detect since it might be too subtle at the beginning, and once it becomes widespread, it can lead to false negatives.

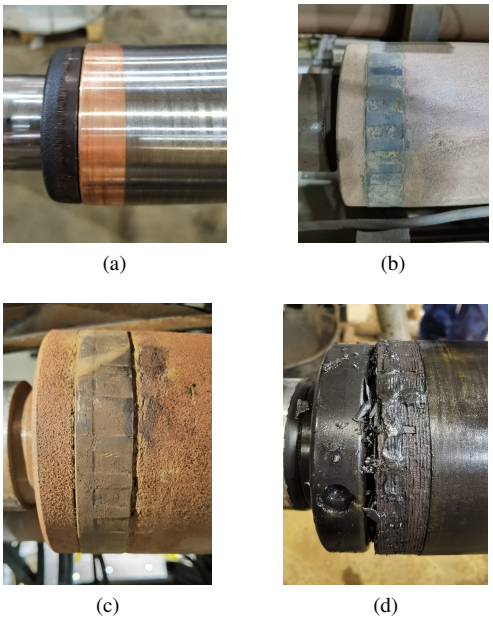

(a) (b) (c) (d)

Fig. 4. Rotor end-rings of deep well submersible motor pumps, in a motor repair shop: new (a) and different wear conditions (b), (c) and (d).

III. Rotor end-ring wear: false negatives.

In this section, the problem of issuing false negatives when diagnosing the wear of end-ring segments in deep well motors through the LSH monitoring is addressed for the first time (LSH is the main rotor asymmetry harmonic, with frequency at $(1-2s)f$ Hz, being f the voltage fundamental component). To serve this purpose, a model of an induction motor (whose parameters are in the Appendix), has been used to study the harmonics present in the current under end-ring wear.

A. Squirrel cage induction model

The dynamic model used in this paper has been implemented in MATLAB and solved using a 4th order Runge-Kutta method with a simulation step size of 10^{-4} s and the following general characteristics: constant air-gap, infinite iron permeability, no saturation and arbitrary number of spatial harmonics considered in inductance and torque calculations.

As for the particular characteristic of the rotor, the electrical equation for the Nth rotor loop can be described as:

$$0 = i_{l(n)}\left(R_{b(n)} + R_{b(n+1)} + R_{uers(n)} + R_{lers(n)}\right) - \\ -i_{l(n-1)}R_{b(n)} - i_{l(n+1)}R_{b(n+1)} - i_{er}R_{lers(n)} + \frac{d\Psi_{l(n)}}{dt} \quad (1)$$

And for the lower end-ring:

$$0 = \sum_{n=1}^{Nr}\left(\left(i_{l(n)} - i_{er}\right)R_{lers(n)} + \frac{d\left(i_{l(n)} - i_{er}\right)}{dt}L_{\sigma lers(n)}\right) \quad (2)$$

Where $i_{l(n)}$ is the current of the Nth rotor loop, i_{er} the end-ring current, $\Psi_{l(n)}$ the total flux linkages of the Nth rotor loop, $R_{b(n)}$ the resistance of bar Nth, $R_{uers(n)}$ and $R_{lers(n)}$ the resistances of the Nth upper end-ring segment and the lower end-ring segment, and $L_{\sigma lers}$ the leakage inductance of the Nth lower end-ring segment.

The wear of an end-ring is modelled as an increase in the impedance of any of its segments. The model input is a three-phase, 400 V, 50 Hz, perfect sinusoidal voltage, sampled at 20 kHz. Finally, one of the resultant currents is processed to analyse the rotor asymmetry harmonics amplitude.

B. *False negatives due to low severity of end-ring wear.*

As stated in the introduction, end-ring faults cause the appearance of the same fault-related harmonics as bar breakages. To simulate the wear of an end-ring segment, the resistance of one of them has been multiplied by 1.25; Fig. 5 shows the spectral density of the simulated line current (in dB with respect to the fundamental component). End-ring wear affects both the resistance and the inductance of the end-ring. In this paper only the resistance is increased to simulate the rotor asymmetry. Nevertheless, the amplitude of the current in the bar progressively decreases, similarly as if the inductance is also increased. Therefore, there is no difference in the rotor asymmetry created in terms of amplitude of the LSH generated, which is the final objective of the analysis.

As can be seen, the main rotor fault harmonics are present (first family Fig. 5a, second family Fig. 5b), but with low amplitudes. Classic rotor fault alarm thresholds use the LSH amplitude: between -45 and -36 dB, incipient failure with even one or two broken bars; above -36 dB, multiple broken bars. As stated through several simulations with this motor, segment resistance must be multiplied by 6.5 and 80 to achieve LSH amplitudes of -45 and -36 dB respectively. On the other hand, a complete segment breakage is more severe than a complete bar breakage: -34 and -38 dB respectively. Concluding, classic LSH thresholds cannot be used if end-ring wear is to be detected before it may be too late to avoid water contamination, as the failure might be too subtle for these limits, thus issuing a false negative.

C. *False negatives in double segments wear.*

The motor has been simulated for all possible combinations of double end-ring segment faults (segments: 1-2, 1-3,...,1-28) in one of the end-rings. The fault is modelled as an increase of 25% in the segment resistance. Since the pattern is repetitive, results are only depicted for one pole pitch (90 mechanical degrees, 7 combinations). Figures 6a and 6b show the amplitude of the LSH and the second family of fault harmonics under double fault, normalized with respect to the amplitude under single fault ($A_{1-2}/A_1, A_{1-3}/A_1, \ldots, A_{1-7}/A_1$) and as a function of the second fault position ($360/28, 2 \cdot 360/28, \ldots, 7 \cdot 360/28$), as well as the theoretical pattern for double bar faults (solid lines) [14]. As can be seen, under double end-ring segments

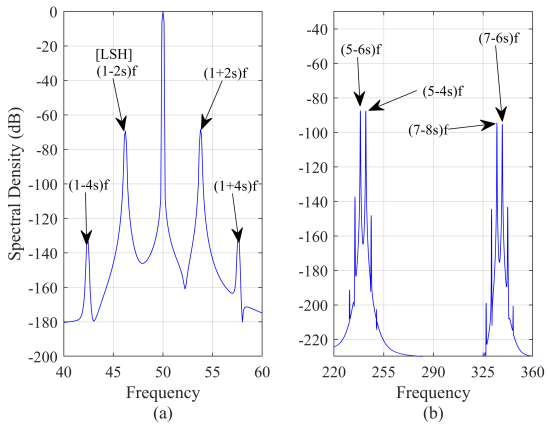

Fig. 5. First (a) and second (b) family of the main harmonics produced by end-ring segment fault (resistance increased by 25%) in the spectrum of the simulated line current of a 4 kW IM operating at 0.038 slip (amplitude in dB with respect to the fundamental component).

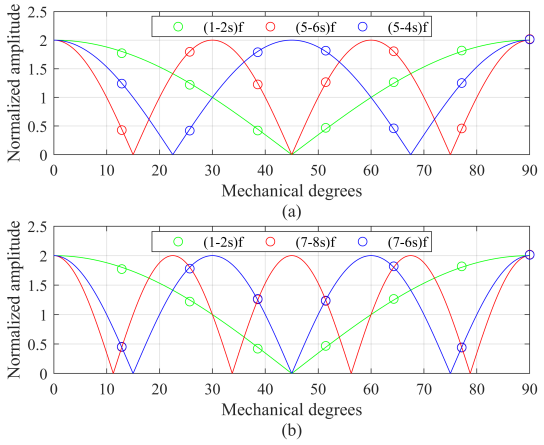

Fig. 6. Theoretical (line) and simulated (circles) amplitude of the main fault harmonics under double faults, normalized with respect to the amplitude under single fault, for each combination of double end-ring segment faults (resistance increased by 25) in one pole pitch; (a): (1-2s)f, (5-6s)f, (5-4s)f ; (b): (1-2s)f, (7-8s)f, (7-6s)f.

faults, the normalized amplitude of the fault harmonics describes the same pattern as in the case of broken bars. Therefore, both cases, end-ring and bar faults, face the same diagnostic problem.

It should be noticed that this problem is of significant importance in the rotor of the submersible motor pumps described in Subsection II, since the degradation of the end-ring weld takes place in different segments, thereby leading to the false negative issues just discussed.

D. *False negatives in multiple segments wear.*

Amplitude patterns for double worn end-ring segments of the previous subsection give an excellent insight into dealing with non-adjacent faults. Nevertheless, as confirmed by visual inspection at the motor repair shop, the friction between the end-rings and the inner cooling-water and the particles

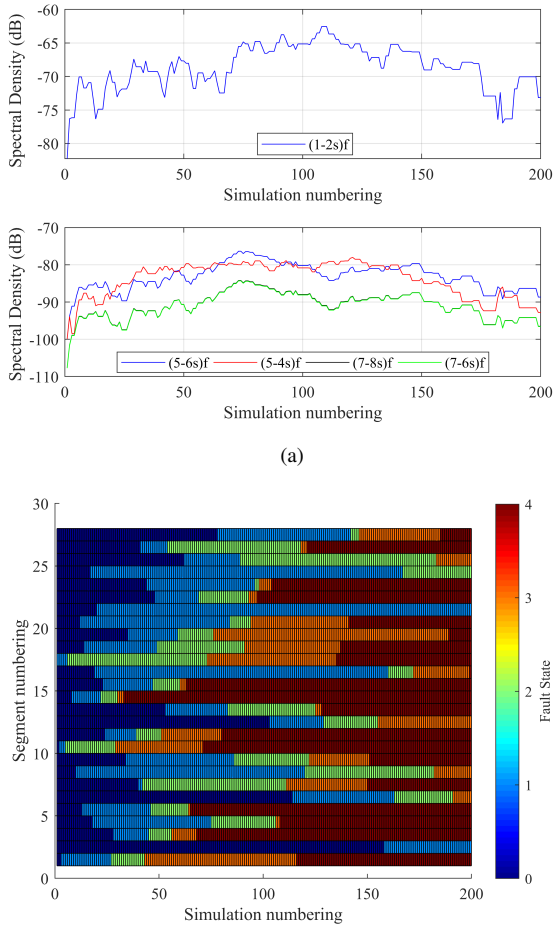

Fig. 7. Amplitude evolution (in dB with respect to the fundamental component) of the main fault harmonics (a) and fault state evolution of each segment of the upper end-ring (b) from the first simulation to simulation #200, in which 75% of the segments have reached their final fault state.

that there might be in it wears the weld in almost every segment but with different severity. Therefore, at least in a first approximation, the wear process can be regarded as a randomly increasing wear of the end-ring segments.

To get an insight on harmonic amplitude patterns in this situation, four fault severity conditions have been defined for each segment of the rotor upper end-ring: resistance increased by 5, 10, 17 and 25%. Then, each segment has randomly gone through the different increasing fault states (e.g., Sim(#1): seg(#17) at fault state 1; Sim.(#2): seg(#17) at fault state 1 and seg(#10) at fault state 1; etc.). Moreover, the process has been designed so that between some consecutive simulations, the rotor fault condition may remain the same (e.g., Sim(#32) and Sim(#33) with the same segments worn and the same severity), as it could happen between consecutive measures in a real case.

Figure 7a shows the amplitude evolution (in dB with respect to the fundamental component) of the main fault harmonics from the first simulation to the simulation #200, in which 75% of the segments have reached their final fault state; Fig. 7b shows the fault evolution of each segment of the upper end-ring for the same range of simulations. As can be seen, the $(5-6s)f$ component has the same pattern as the component at $(7-6s)f$, while both are different from the $(5-4s)f$ pattern. It should be noticed as well that, for this particular number of rotor bars, the harmonic at $(7-8s)f$ describes the same evolution as the ones at $(5-6s)f$ and $(7-6s)f$. These results are in agreement with those shown in Fig. 6 for double faults.

It can be concluded from Fig. 7a, that a long period condition monitoring (e.g., biannual measurements) based exclusively on the LSH followup can be especially unreliable for this wear process since its amplitude is always under classic rotor damage thresholds, being even nearly as low as in a healthy state when 75 % of the segments are damaged. Although the same problem might also be encountered with multiple non-adjacent broken bars (principally in HV machines with frequent transient stresses [13], [21]), the number of broken elements is small when compared to the number of segments that deteriorate in the rotors described in this paper. Therefore, given the extra difficulties with respect to non-adjacent broken bars, it is of particular interest for these machines to develop a reliable indicator to monitor the end-ring condition.

IV. Experimental Results

The purpose of this section, which can be achieved by performing the test with a standard induction motors, is: first, an understanding of the behaviour of the rotor asymmetry harmonics under multiple and progressive segment degradation, and second, a procedure to identify that a fault is in progress in a real motor. Testing a submersible motor would require a well, a pump coupled to the motor, a crane to put the motor inside the well and a system of pipelines and valves to regulate the load. The critical aspect that prevents to test this type of motor outside a well is the surrounding water going inside the pump inlet to create convection heat transfer which cools the motor and avoids over-heating. Since these means cannot be found in an academic lab, a standard squirrel cage induction motor (2.2 kW, 2-p, 28-bars, 230 V, 8.5 A, 1420 rpm, Δ connection, line-fed) is tested instead, under several fault states. More precisely, two identical induction motors are coupled by their shafts, one fed by the grid, and the other by a frequency converter. By decreasing the feeding frequency of the second machine, the tested motor is driven to its rated load. Then, the line current is measured to perform MCSA. Finally, the conclusions about motors behaviour under the end-ring degradation acquired with standard motors are verified with submersible pump motors in the real field cases shown in the next section.

Why not using vibrational analysis? It is hard to be performed in deep-well submersible motors, as it requires to place the sensors in the body of the machine, which in this case is located inside an aquifer up to 500 m depth. The long data transmission cable hinders the measurements,

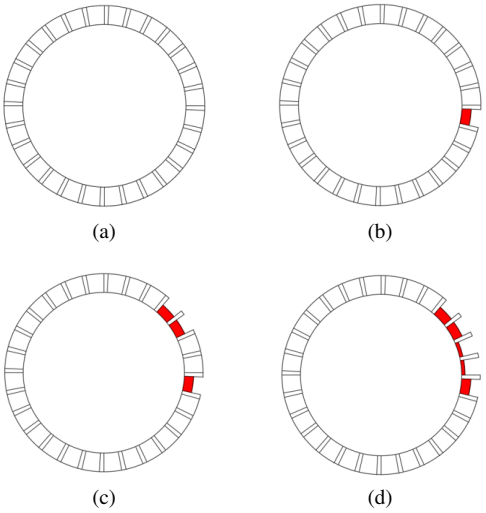

Fig. 8. Transversal section of the end-ring, showing the segments between the bars, and the progressive fault tested: healthy (a), segment 1 drilled 11 mm (b), segments 1, 4 and 5 drilled 11 mm (c) and finally drilling 14 mm in segments 2 and 3 (d).

since it introduces capacitances into the sensor circuit distorting the vibration signal. Moreover, it is difficult to find a sensor robust enough to deal with such a harsh environment: underwater operation with dirt, mud, etc. Therefore, only Pt-100 temperature sensors, with motors especially designed to place the sensor inside the sealed motor, are used at these depths by water distribution system operators.

After testing the motor in a healthy state, holes have been drilled in different end-ring segments between the bars (as seen in Fig. 8). Segment 1 has been drilled to 11 mm depth out of 18.5 mm. Then, to compensate for the rotor asymmetry, segments 4 and 5 have been worn (exact compensation would be between these two segments) by producing holes of smaller amplitudes but similar depths (11 mm). Finally, segments 2 and 3 have also been worn with 14 mm deep holes. Figure 9 shows the final rotor state.

Figure 10 shows the LSH amplitude(in dB with respect to the fundamental component) in the line current spectrum for these four states with the motor operating at 100 % of rated load. It can be seen how after the wear of segments 1, 4 and 5, the LSH amplitude is even smaller than when the motor was healthy. Moreover, when comparing fault state 1 (only segment 1 worn) with fault state 3 (segments 1, 2, 3, 4 and 5 worn), it is observed that the amplitude of the LSH is approximately the same. In none of the faulty states, the LSH reaches an amplitude usually considered as the starting of a rotor fault (-45 dB), even if the rotor has been seriously damaged, as seen in Fig. 9. Therefore, a single measurement of the LSH amplitude would not raise the alarm on the rotor condition in any of these four states. Moreover, even for severe faulty conditions, the indicator might be the same as in the healthy state due to asymmetry cancellation. Concluding, a single measurement of the LSH in a faulty rotor will cause a false negative.

Figure 11a shows the evolution of the LSH amplitude,

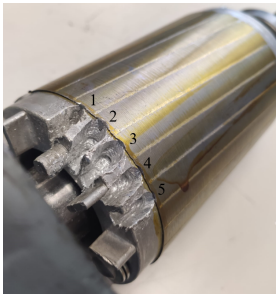

Fig. 9. Rotor after wearing end-ring segments 1, 4 and 5 (11 mm deep hole), and segments 2 and 3 (14 mm deep hole).

from the healthy state to the wearing of the segments 1 to 5, passing through the two intermediate faulty states (only segment 1 worn and segments 1, 4, 5 worn). For each state, five measurements at full load are shown. Figure 11b shows that same result related to four other rotor fault harmonics, selected, as explained in Section III, for having significantly different amplitude patterns against double faults. These laboratory results emulate the periodic monitoring of a field motor.

The analysis of the LSH amplitude from time to time measurements would not provide enough valuable information. The rotor would be categorised healthy, considering that, for every case analysed, the LSH amplitude is significantly lower than the early stage alarm threshold (-45 dB) commonly used in industry. Nevertheless, the time evolution of the LSH amplitude clearly shows that a rotor failure is developing: changes of 7 to 10 dB are observed, while, as analysed in the lab, load oscillations generate changes of only 0.5 dB approximately. If the measurements are from a deep-well motor, where end-ring wear is likely to occur, these changes are sufficient to alert maintenance personnel that a failure is occurring. Therefore, it is not important in these motors how large the LSH is, especially knowing that a severe fault might not show up as a large LSH since the rotor asymmetry might cancel out. Concluding, new alarm thresholds should be defined related to the rate of change in the LSH amplitude for this type of motors.

Concerning the evolution of the harmonics shown in Fig. 11 (down), the $(5-4s)f$ (red) is especially important: at the healthy state, the amplitude oscillates between -85 to -81 dB, increasing to -79 dB in the first faulty state, increasing again to -75 dB in the second faulty state (when LSH decreases to healthy state values) and finally decreasing to -78 dB in the last state (when LSH increases back to -52.5 dB). Therefore, it is a good complement for the LSH monitoring to detect the end-ring wear. On the other hand, the evolutions of the harmonics depicted in blue and black also show different complementary patterns, not decreasing that much as the LSH in the third state but also maintaining their amplitudes at the final state. Finally, the pattern of the harmonic plotted in green does not seem to give significant information.

Finally, it is worth noting that the operation of the motor in the harsh environment of a deep well does not affect

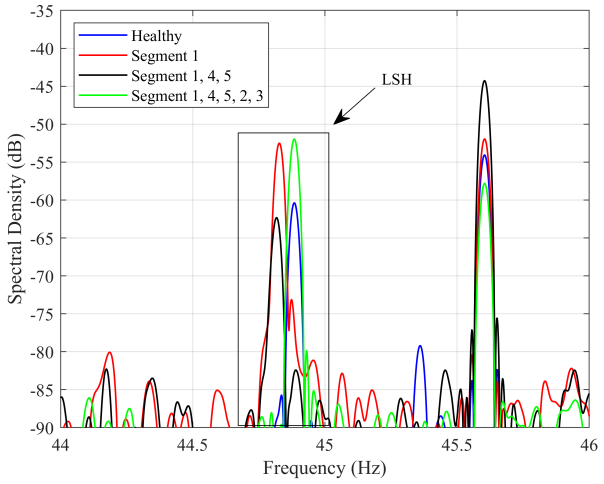

Fig. 10. LSH amplitude in the line current spectrum for the four fault states tested (in dB with respect to the fundamental component).

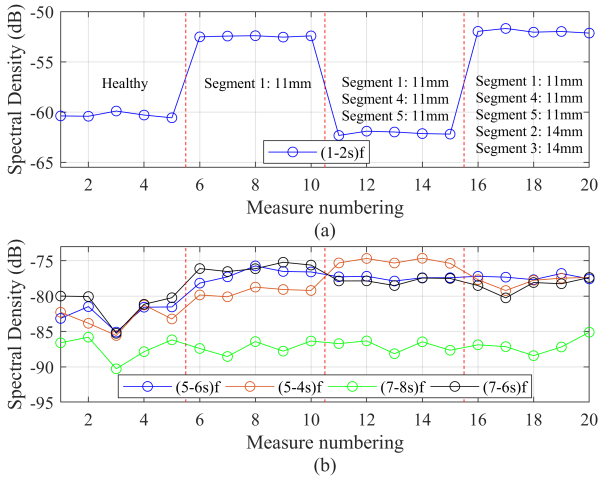

Fig. 11. Lab emulation of a field periodic monitoring of the LSH amplitude (a) and four significant rotor fault harmonics (b): five measurements per fault state, separated with vertical dotted lines."

the proposed indicator. The motor is sealed to prevent from contamination, and it is designed with pressure stabilizer; therefore, only changing temperature might affect the inside. The aquifer in which the motor is submerged at a high depth tends to stabilize the temperature. Changes might appear as the year seasons take place, load increases, or malfunctioning appears (that is why Pt-100 temperature sensors are installed inside high power motors). Nevertheless, a temperature change would affect the whole rotor, without increasing its asymmetry. Therefore, changes in the LSH amplitude will only be related to an increase in end-ring wear.

V. Field Cases

Two deep well motors from two different pumping stations are continuously monitored, measuring all their startups and a steady-state every six operating hours (500 s each). FFT is used to calculate the current spectrum, and faulty harmonics are localized and their amplitudes quantified.

A. Field case 1

The first motor is a Caprari M12230 (230 HP, 1-p, 30 bars, 380 V, 335 A, 2950 rpm), fed with a frequency converter (model SD7058055 from Power Electronics), installed in a deep well at 118.87 m from the ground. Figure 12 shows the time evolution (a measure every six operating hours) of the LSH amplitude (in dB with respect to the fundamental component) during nearly a year (2020). Horizontal dotted red lines represent the thresholds used in the industry to consider the appearance of bar breakages: between -45 and -36 dB, incipient failure with even one or two broken bars; above -36 dB, multiple broken bars. The data gaps in the middle of March, end of June, and end of August are periods in which problems with the remote control of the measurement equipment could not be rapidly solved due to the Covid situation.

As can be seen, the LSH amplitude starts to increase slowly very soon from the first measurement and, in approximately two and a half months, surpasses the -45 dB threshold. Then, in the middle of May (one month later), it increases very quickly to -40 dB, to suddenly drop to -44 dB after a month. Then, the tendency is to slowly but continuously increase until reaching -36 dB in October and approximately keep this level until descending again in November to -40 dB. This ratio of change in the LSH amplitude indicates the presence of severe end-ring wear. In addition, during the last month, stator winding fault harmonics $(n(1-s)/p \pm k)f$ increased dramatically as shown in Fig. 13. The pump replacement can be finally planned; the motor is drawn from the well at 118.87 m and send to the motor repair shop.

Figures 14a and 14c show two different perspectives of the rotor upper end-ring (near the coupling with the pump), while Figs. 14b and 14d show two different perspectives of the lower end-ring (at the bottom part of the motor-pump set). It can be observed how both end-rings have lost most of the copper liquid soldering: the copper sheets can be observed, even distinguishing the position of the copper bars (opposite to the healthy rotor shown in Fig. 4a). The upper end-ring is particularly damaged, with parts of the copper sheets detached, exposing some copper bars. In the lower end-ring, some material has been settled in the lower part of the side shown in Fig. 14d (probably due to gravitation).

The unequal end-rings wear in their different perspectives explains the changes in the LSH amplitude: when some material is detached from some part of the end-ring, its asymmetry increases, while it balances when the rest is worn too. Not only the end-ring is worn, but also its contact with the bars through the loss of the copper liquid soldering that glues end-ring sheets and bars together, and the degradation of the end-ring sheets itself, particularly at the contact position with the bars, even exposing the bars which are covered initially. The ratio of change in the LSH enabled the fault detection and the motor replacement.

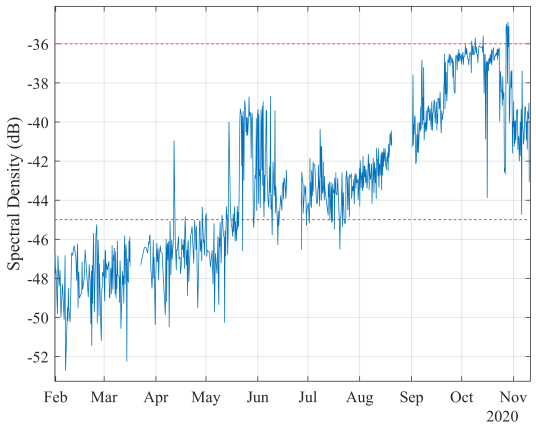

Fig. 12. Time evolution (a measure every 6 operating hours) of the LSH amplitude (in dB with respect to the fundamental component) of the first pumping station motor continuously monitored.

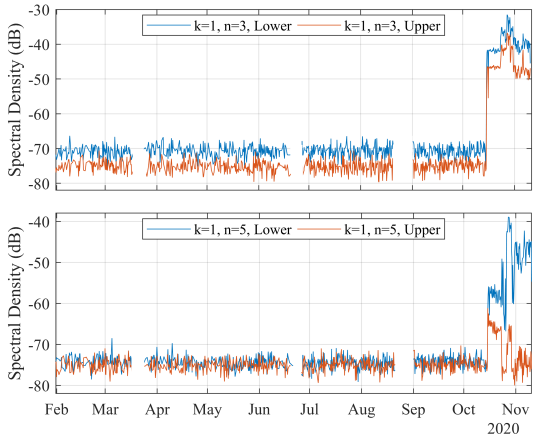

Fig. 13. Time evolution (a measure every 6 operating hours) of the stator winding fault harmonics amplitude (in dB with respect to the fundamental component) of the first pumping station motor continuously monitored.

Unfortunately, the material detached from the end-ring polluted the water that internally cools the motor. Since the water, propelled by the rotor, rotates at high speed, suspended particles are naturally shoot to the inner part of the stator. Some of these particles might impact the winding, breaking the insulation, which is what usually happens when parts of a rotor bar are detached in standard copper rotor induction motors. Therefore, this is probably the cause of the stator winding insulation degradation, also detected in Fig. 13: the stator insulation resistance (measured in the motor repair shop) was below the company quality standards, prompting the stator rewinding.

It is worth to conclude that, continuously monitoring changes in the LSH amplitude can reveal early stage degradation of the rotor. Nevertheless, since the liquid soldering can be easily replaced in the motor repair shop, the true objective is to prevent the appearance of winding damages, caused by the detached rotor particles suspended in the internally cooling water, which propelled by the rotor might impact the stator, causing damage expensive to be repaired.

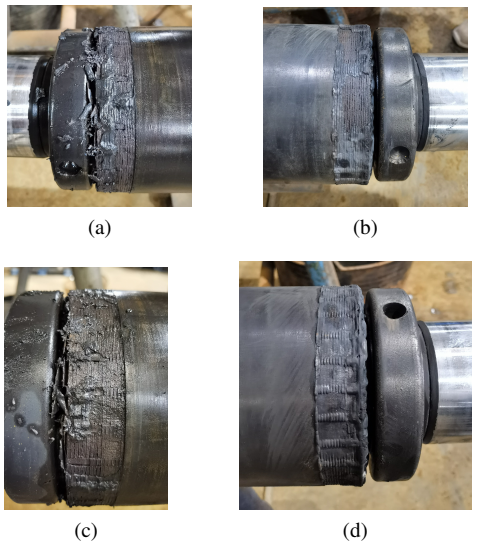

Fig. 14. Worn rotor end-rings (upper in (a) and (c) and lower in (b) and (d)), of the first motor being monitored and repaired in the motor repair shop.

B. Field case 2

The second motor is an Aturia N12-340 (340 HP, 1-p, 28 bars, 380 V, 475 A, 2900 rpm), fed with a soft-starter (model V50900 from Power Electronics) and installed in a deep well at 170.3 m from the ground. Figure 15 shows, from top to bottom, the time evolution of the LSH, the $(5-6s)f$ and the $(7-6s)f$ amplitudes (in dB with respect to the fundamental component) during nearly a year (2020). In this case, the LSH remains below the lower band of the classic LSH thresholds (-45 dB) during the whole period. However, as can be seen, from June onwards, the typical pattern of ups and downs begins to be observed. The LSH amplitude slowly decreases from -58 to -63.5 dB in August. Then, it goes up to -61.5 dB, where it remains stable until the end of September, when it reaches -59.7 dB. Finally, in the last month, several sharp changes are reported with variations between -2 and -4 dB. This could mean that the end-ring wear is developing. The pattern is even more evident with the $(5-6s)f$ and the $(7-6s)f$ harmonics, particularly in the latter, as the change ratio goes from 5 to 20 dB. Finally, it should be noted that the $(5-6s)f$ and $(7-6s)f$ patterns are very similar, which is in line with what has been shown in the previous sections.

The first intention was to continue monitoring this motor until the failure was more advanced. Unfortunately, the coupling between the motor and the pump broke down at the end of October, and as a result, the motor had to be drawn. Nevertheless, thanks to the continuous monitoring, it was possible to warn the company that an eccentricity problem was taking place, so they could make arrangements to avoid an unscheduled outage. The increase in eccentricity was detected by measuring the Upper Mixed Eccentricity Harmonic (UMEH): $(1+(1-s)/p)f$; lower harmonic is

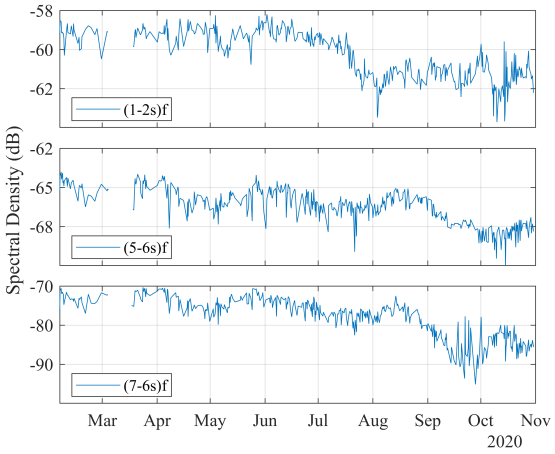

Fig. 15. Time evolution (a measure every 6 operating hours) of the rotor asymmetry harmonic amplitudes (in dB with respect to the fundamental component) of the second pumping station motor continuously monitored.

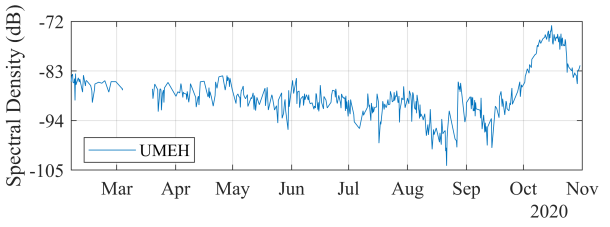

(a)

(b) (c) (d)

Fig. 16. Time evolution (a measure every 6 operating hours) of the UMEH (in dB with respect to the fundamental component) of the second pumping station motor continuously monitored (a); photos of the broken coupling between the motor and the pump: part attached to the motor from two different perspectives (b) and (c) and part to be connected to the pump (d).

not usually detected in this type of motor (it might also be removed when filtrating the DC component, due to its proximity). Figure 16a shows the UMEH time evolution and how, in the middle of September, the amplitude began to increase. Contrary to the LSH, eccentricity harmonics do not have a universally accepted threshold to correlate the UMEH amplitude with a certain degree of eccentricity. Nevertheless, the sudden change in its amplitude explains well what was finally analysed in the motor repair shop. Figures 16b, 16c and 16d show the eventually broken down coupling between the motor and the pump. When the coupling breaks down, the forces that create the eccentricity highly decrease, and the rotor goes back to its natural position: that is why the UMEH amplitude decreases at the end of 16a. Since the motor is in the lower part of the system (Fig. 3), it receives the weight of all the water and the pump. Therefore, friction between the two broken shafts is high, and the pump stills rotating.

VI. Conclusions

Deep well submersible pump motors have a specific rotor end-ring manufacturing process: copper laminations with punching holes to place the bars, are glued to the end of these rotor bars with copper liquid soldering. Internally cooling water, which propelled by the rotor moves at a high speed, erodes the liquid soldering. Therefore, a particular type of fault appears, widespread in these motors: the end-ring wear, documented in this paper through several motor repair shop cases. The water suspended particles that end-ring wear generates, are impelled by the centrifugal force, and might impact the stator winding, causing serious damage.

As has been shown through simulation, lab tests, and field cases, a LSH monitoring with long periods between measurements (e.g., biannual) is insufficient for end-ring wear detection. First, in a single amplitude measurement, the wear might not be enough to raise the LSH amplitude to a level considered as faulty according to traditional rotor fault indicators. Second, once the wear spreads, rotor asymmetry might even be cancelled by multiple segments wear, lowering the LSH amplitude.

Continuous monitoring is needed to solve the problem: two field motors have been daily measured during nearly a year. Moreover, a new paradigm must be considered when monitoring deep well induction motors: the ratio of change in the LSH amplitude must be used as an indicator of end-ring wear, even if classic LSH thresholds are not reached (-45 dB). As shown through the field cases results, a changing LSH amplitude in time reveals the degradation of an end-ring. More precisely, ups and downs in the LSH amplitude reveal that the rotor asymmetry first increases and then is compensated as all the segments in the end-ring are equally worn. Therefore, instead of comparing the LSH amplitude with classic thresholds, changes in its amplitude must be monitored.

Changes in the secondary fault harmonics properly chosen are very useful to complement the LSH monitoring. Finally, stopping the motor at an early stage of end-ring wear might prevent this fault from contaminating the water that internally cools this type of motor and creates important secondary damage, as the winding failure that might appear if contaminating particles impact its coils at a high speed.

Appendix: Simulated Motor Data

General	U = 400 V, Connection = Y, N_{bars} = 28 p = 2, h = 27, T = 26.6 Nm, J= 0.030 kg/m^2
Stator	R = 1.25 Ω , L_σ =3.57 mH, L_μ = 191.4 mH
Rotor	R_{bar} = 0.07 mΩ, $L_{\sigma,bar}$ =0.28 µH, L_μ = 5.6 µH R_{ring} = 0.05 mΩ, $L_{\sigma,ring}$ = 0.05 µH

ACKNOWLEDGMENT

This work was supported by the Universitat Politècnica de València and the Spanish Ministry of Science, Innovation and Universities [FPU19/02698].

We would also like to thank FACSA for granting access to their facilities in order to conduct the field cases measurements and especially Miguel Ortiz-Gomez and Juan Miguel Llopis-Gomez for assisting us in the process.

REFERENCES

[1] W. R. Finley and M. M. Hodowanec, "Selection of copper versus aluminum rotors for induction motors," *IEEE Transactions on Industry Applications*, vol. 37, no. 6, pp. 1563–1573, 2001.

[2] J. Pons-Llinares, D. Morinigo-Sotelo, O. Duque-Perez, J. Antonino-Daviu, and M. Perez-Alonso, "Transient detection of close components through the chirplet transform: Rotor faults in inverter-fed induction motors," in *IECON 2014 - 40th Annual Conference of the IEEE Industrial Electronics Society*, 2014, pp. 3386–3392.

[3] L. Beneduce, G. Caruso, D. Lannuzzi, E. Pagano, and L. Piegari, "Analysis of a structural faiulure mode arising in cage rotors of induction machines," *Electrical Engineering*, vol. 93, pp. 179–191, 2011.

[4] M. Jeong, J. Yun, Y. Park, S. B. Lee, and K. N. Gyftakis, "Quality assurance testing for screening defective aluminum die-cast rotors of squirrel cage induction machines," *IEEE Transactions on Industry Applications*, vol. 54, no. 3, pp. 2246–2254, 2018.

[5] S. Nandi, H. A. Toliyat, and X. Li, "Condition monitoring and fault diagnosis of electrical motors—a review," *IEEE Transactions on Energy Conversion*, vol. 20, no. 4, pp. 719–729, 2005.

[6] H. Weichsel, "Squirrel-cage rotors with split resistance rings," *Transactions of the American Institute of Electrical Engineers*, vol. 47, no. 3, pp. 929–936, 1928.

[7] S. Williamson and A. C. Smith, "Steady-state analysis of 3-phase cage motors with rotor-bar and end-ring faults," *IEE Procedings B (Electric Power Applications)*, vol. 129, no. 3, pp. 93–100, 1982.

[8] H. A. Toliyat and T. A. Lipo, "Transient analysis of cage induction machines under stator, rotor bar and end ring faults," *IEEE Transactions on Energy Conversion*, vol. 10, no. 2, pp. 241–247, 1995.

[9] J. F. Bangura and N. A. Demerdash, "Diagnosis and characterization of effects of broken bars and connectors in squirrel-cage induction motors by a time-stepping coupled finite element-state space modeling approach," *IEEE Transactions on Energy Conversion*, vol. 14, no. 4, pp. 1167–1176, 1999.

[10] S. J. Manolas and J. A. Tegopoulos, "Analysis of squirrel cage induction motors with broken bars and rings," *IEEE Transactions on Energy Conversion*, vol. 14, no. 4, pp. 1300–1305, 1999.

[11] T. J. Sobczyk and W. Maciolek, "Does the component (1-2s)f0 in stator currents is sufficient for detection of rotor cage faults?" in *2005 5th IEEE International Symposium on Diagnostics for Electric Machines, Power Electronics and Drives*, 2005, pp. 1–5.

[12] C. Kral, H. Kapeller, J. V. Gragger, A. Haumer, and B. Kubicek, "Phenomenon rotor fault — multiple electrical rotor asymmetries in induction machines," in *2009 IEEE International Symposium on Diagnostics for Electric Machines, Power Electronics and Drives*, 2009, pp. 1–9.

[13] M. Riera-Guasp, M. F. Cabanas, J. A. Antonino-Daviu, M. Pineda-Sánchez, and C. H. R. García, "Influence of nonconsecutive bar breakages in motor current signature analysis for the diagnosis of rotor faults in induction motors," *IEEE Transactions on Energy Conversion*, vol. 25, no. 1, pp. 80–89, 2010.

[14] M. Riera-Guasp, J. Pons-Llinares, F. Vedreño-Santos, J. A. Antonino-Daviu, and M. Fernández Cabanas, "Evaluation of the amplitudes of high-order fault related components in double bar faults," in *8th IEEE Symposium on Diagnostics for Electrical Machines, Power Electronics Drives*, 2011, pp. 307–315.

[15] V. Climente-Alarcon, J. A. Antonino-Daviu, A. Haavisto, and A. Arkkio, "Evolution of high order fault harmonics during a bar breakage with compensation," in *2014 International Conference on Electrical Machines (ICEM)*, 2014, pp. 1888–1893.

[16] J. A. Antonino-Daviu, K. N. Gyftakis, R. Garcia-Hernandez, H. Razik, and A. J. Marques Cardoso, "Comparative influence of adjacent and non-adjacent broken rotor bars on the induction motor diagnosis through mcsa and zsc methods," in *IECON 2015 - 41st Annual Conference of the IEEE Industrial Electronics Society*, 2015, pp. 001 680–001 685.

[17] K. N. Gyftakis, J. A. Antonino-Daviu, and A. J. Marques Cardoso, "A reliable indicator to detect non-adjacent broken rotor bars severity in induction motors," in *2016 XXII International Conference on Electrical Machines (ICEM)*, 2016, pp. 2910–2916.

[18] J. Antonino-Daviu, H. Razik, A. Quijano-Lopez, and V. Climente-Alarcon, "Detection of rotor faults via transient analysis of the external magnetic field," in *IECON 2017 - 43rd Annual Conference of the IEEE Industrial Electronics Society*, 2017, pp. 3815–3821.

[19] P. A. Panagiotou, I. Arvanitakis, N. Lophitis, J. A. Antonino-Daviu, and K. N. Gyftakis, "A new approach for broken rotor bar detection in induction motors using frequency extraction in stray flux signals," *IEEE Transactions on Industry Applications*, vol. 55, no. 4, pp. 3501–3511, 2019.

[20] M. E. Iglesias-Martínez, P. Fernández de Córdoba, J. A. Antonino-Daviu, and J. A. Conejero, "Detection of nonadjacent rotor faults in induction motors via spectral subtraction and autocorrelation of stray flux signals," *IEEE Transactions on Industry Applications*, vol. 55, no. 5, pp. 4585–4594, 2019.

[21] Y. Park, H. Choi, S. B. Lee, and K. N. Gyftakis, "Search coil-based detection of nonadjacent rotor bar damage in squirrel cage induction motors," *IEEE Transactions on Industry Applications*, vol. 56, no. 5, pp. 4748–4757, 2020.

[22] T. Ishikawa, S. Shinagawa, and N. Kurita, "Analysis and failure diagnosis of squirrel-cage induction motor with broken rotor bars and end rings," *IEEJ Journal of Industry Applications*, vol. 2, no. 6, pp. 292–297, 2013.

[23] J. Bonet-Jara, D. Morinigo-Sotelo, O. Duque-Perez, L. Serrano-Iribarnegaray, J. M. Llopis-Gomez, M. Ortiz-Gomez, and J. Pons-Llinares, "End-ring wear in deep well submersible motor pumps," in *2021 IEEE 13th International Symposium on Diagnostics for Electrical Machines, Power Electronics and Drives (SDEMPED)*, vol. 1, 2021, pp. 79–85.

VII. BIOGRAPHIES

Jorge Bonet-Jara received the M.Sc degree in Industrial Engineering and the Master in Electrical Engineering from the Universitat Politècnica de València (UPV, Spain), in 2016 and 2018, respectively. He is currently carrying out his Ph.D in Fault Diagnosis and Sensorless Speed Estimation in the Electric Engineering Department of the UPV. His research interests include condition monitoring, and modelling of electrical machines.

Daniel Morinigo-Sotelo(M'04) received the B.S. and Ph.D. degrees in electrical engineering from the University of Valladolid (UVA), Spain, in 1999 and 2006, respectively. He is currently with the research group on Analysis and Diagnostics of Electrical Grids and Installations (ADIRE), that belongs to the ITAP Institute (UVA), and with the HSPdigital Research Group, Mexico. His current research interests include fault detection and diagnostics of induction machines, power quality, and smart grids.

Oscar Duque-Perez is an associate professor of Electrical Engineering at the University of Valladolid (UVa), Spain. He received his B.S. and Ph.D. degrees in electrical engineering from UVa, in 1992 and 2000, respectively. He is a member of the research group on Analysis and Diagnostics of Electrical Grids and Installations (ADIRE) and ITAP, University of Valladolid. His main research fields are electric machines condition monitoring, power systems reliability and power quality, and electric energy efficiency.

Luis Serrano-Iribarnegaray received the M.Sc. degree in Industrial Engineering from the Escuela Técnica Superior de Ingenieros Industriales de Bilbao (1971) and the Ph.D. degree in Electrical Engineering from the Universitat Politécnica de Madrid (1978). He is Full Professor in the Electrical Engineering Department of the Universitat Politècnica de València since 1982, where he now works as Professor Emeritus. His research interests are theory, control and diagnosis of electrical machines.

Joan Pons-Llinares(M'13) is currently an Associate Professor in the Electric Engineering Department of the UPV.